공학석사 학위논문

Multiscale Modeling Approach for Glassy Polymer Using Molecular Dynamics Simulations and Micromorphic Theory

분자동역학과 마이크로몰픽 이론을 이용한 유리상 고분자의 멀티스케일 모델링 방법

2020 년 8 월

서울대학교 대학원

항공우주공학과 항공우주공학전공

박 찬 욱

Multiscale Modeling Approach for Glassy Polymer Using Molecular Dynamics Simulations and Micromorphic Theory

분자동역학과 마이크로몰픽 이론을 이용한 유리상 고분자의 멀티스케일 모델링 방법

지도 교수 윤 군 진

이 논문을 공학석사 학위논문으로 제출함

2020 년 8 월

서울대학교 대학원

항공우주공학과 항공우주공학전공

박 찬 욱

박찬욱의 공학석사 학위논문을 인준함

2020 년 8 월

위 원 장 김 지 환 (인)

부위원장 윤 군 진 (인)

위 원 김 용 협 (인)

Abstract

Multiscale Modeling Approach for Glassy Polymer Using Molecular Dynamics Simulations and Micromorphic theory

Chanwook Park
Department of Aerospace Engineering
Aerospace Engineering Major
The Graduate School
Seoul National University

This thesis starts with an investigation on the strain rate discrepancy of tensile experiments and molecular dynamics (MD) simulations for glassy polymers. It is postulated that MD tensile simulations conducted under super-fast strain rates represent the nanoscale craze region in the macro tensile specimen. By comparing the ductile-brittle transition of glassy polymers at experiments and simulations, the postulation is validated resulting in a conclusion that to understand the constitutive relation of a glassy polymer by using

the MD simulation, a multi-scale continuum approach must be employed which can incorporate MD results as the physics of the micro (or nano) scale. For this purpose, the two-scale micromorphic theory is adopted where tensile experimental results are applied to the macro-scale and MD results are applied to the micro-scale. With a proper choice of the length parameter of the micro-scale, the length scale of the continuum model became compatible with MD RUC. Finally, the multi-scale model exhibited the distinctive ductile and brittle plastic deformation when given with ductile and brittle MD s-s curves respectively. Since it also returns the dynamic response from the s-s curves, the time-scale and the strain rate of the MD simulations and the continuum model can be comparable by choosing proper model parameters. This multi-scale approach is expected to be an essential method for the scale bridging between the nanomechanics and the continuum mechanics.

Keywords : Multiscale simulation, molecular dynamics, glassy polymer, ductile-brittle transition, micromorphic theory

Student Number : 2018-27299

Table of contents

List of figures

List of tables

1. Introduction

1.1. Background and motivation

Studies on polymeric nanocomposites aided by molecular dynamics (MD) simulations have proliferated over the past year [1-4]. In particular, tensile simulations have been extensively conducted on MD simulations, which are expected to replace conventional mechanical tensile tests performed in experiments [5-8]. In the meanwhile, the time scale discrepancy between MD simulations (~nano seconds) and real-time experiments, and the following huge gap of strain rates have been a recurring issue among researchers [9]. Most MD tensile strain rates are extremely fast (in the range of 10^{7}~10^{10}/s) whereas conventional tensile experiments are conducted under the quasi-static condition. To resolve this, a time-shifting method have been extensively exploited [10-12]. For instance, Odegard et al.[10] conducted uniaxial tensile tests on thermoset polymers with various strain rates (~10^{9} /s) to obtain young's modulus and yield strength. Then they co-plotted the results with experimental results obtained under a quasi-static strain rate where they could define a relationship between strain rates and

mechanical properties. Park et al.[11] took one step further where they generated a global curve of the yield stress of thermoset polymers using the time–temperature superposition and Eyring theory [13]. They predicted the quasi–static yield stress of epoxy resin from the global curve of yield stress which was obtained from the temperature–accelerated MD simulation.

The shifting methodology described above is based on a premise that the representative unit cell (RUC) in MD simulations can effectively represent the macroscale specimen under the periodic boundary condition (PBC). That is, they assume the macro specimen consists of duplicates of the same MD RUC. This premise seems reasonable in the elastic regime since they yielded accurate predictions about experimental results or the discrepancy between simulations and experimental results [12]. In the plastic regime, however, most materials (especially polymeric materials) deform heterogeneously, which means that the assumption of homogeneous deformation no longer holds [14]. When a macro specimen undergoes the plastic deformation, there is a local region where the plastic yield happens while the other regions are still in the elastic regime. A

single MD RUC in the nanoscale never succeed to depict the heterogeneous deformation of polymeric materials and this is the reason why most attempts to discover the yield criteria of glassy polymers using MD simulations have failed to bridge the gap between simulations and experiments [15]. Therefore, one must scrutinize the inhomogeneous deformation scheme when dealing with the plastic deformation of polymeric materials. This thesis scrutinizes the inhomogeneous deformation mechanism of glassy polymers as well as the time and length scale discrepancy between MD simulations and conventional tensile experiments.

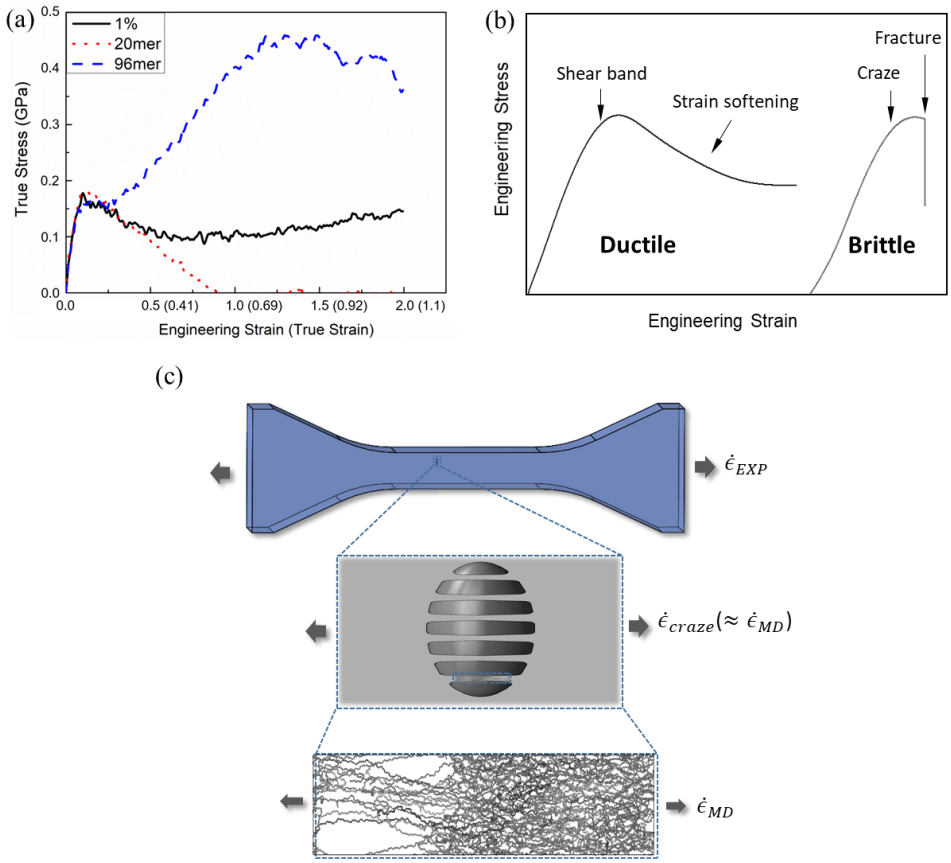

Figure 1 Meaning of the strain rate discrepancy between MD simulations and tensile experiments. (a) MD s-s curves of tensile simulations performed under super-fast strain rate. 1% case is the radical-polymerized sample and 20mer/90mer cases are the representative molecule models with chain length or 20 mer and 90 mer, respectively. Reproduced with permission.[16] (b) Typical s-s curves for the brittle fracture with the craze yielding (left) and the ductile failure with the shear band (right). The curves are from tensile experiments conducted in this thesis. (c) Schematic illustration of a macro tensile specimen with an extended view of the nanoscale craze region. It is postulated that the MD RUC represents the nanoscale craze region in the macro tensile specimen.

1.2. Objectives and research significance

To handle this, our group first studied on realistic modeling of thermoplastic polymers. An algorithm was developed that can realize the whole process of polymerization; initiation, propagation, and termination [16–18]. Through this algorithm, a poly(methyl methacrylate) (PMMA) RUC with a molecular weight of ~14,000 g/mol was grown from a mixture of monomers and initiators. A tensile simulation under a super–fast strain rate (2×10^9/s) was performed on the MD RUC to obtain the stress–strain curve (s–s curve), which is shown in Figure 1 (a) as a black solid line denoted by 1% on the legend. The s–s curve shows an initial yield point followed by the strain softening and hardening, which is similar to the tensile behavior of a ductile glassy polymer. At this point, it is easy to conclude that the MD RUC successfully depicts the real–time deformation mechanism of the glassy polymer. However, it has a serious fallacy. The MD RUC is not ductile in the current simulation; instead, it is brittle [19, 20]. To dig deeper into this situation, the deformation mechanism of thermoplastic glassy polymers must be elucidated.

Glassy polymers deform in two different ways; ductile and brittle.

It is widely known that the ductile deformation is induced by the shear yielding while the brittle deformation is dominated by the craze yielding [21, 22]. As can be seen in Figure 1(b), the strain softening in the ductile s-s curve is dominated by the shear band mechanism. In MD s-s curve, on the other hand, the strain softening on the 1% model (Figure 1(a) black solid line) is not a manifestation of the shear banding even though the shape of the s-s curve is similar to that of the ductile case in Figure 1(b). Instead, the softening in MD s-s curve is induced by the craze initiation, which dominates the brittle deformation [19, 20, 23]. After the initial yield, in MD RUC, a void is nucleated due to the craze initiation under the super-fast strain rate. As the void grows, polymer chains near the void gain enough space to release stress [16, 19, 20]. Then, how can one explain the ductile-like s-s curve (but brittle, in fact) in MD simulation conducted under a super-fast strain rate?

It has been pointed out that the glassy polymer deforms heterogeneously in the plastic regime. When the polymer undergoes a brittle deformation, nanoscale crazes inside a macro specimen stretch extremely fast and elongate a lot (typical values of the

extension ratio of a craze ranges from two to seven) [19], although the macro specimen is stretched by a quasi-static strain rate as depicted in Figure 1 (c). Hence it is obvious that the strain and strain rate of the macro specimen and the nanoscale craze region are different in nature, and strain rates between the two different scales ($\dot{\epsilon}_{EXP}$ and $\dot{\epsilon}_{craze}$) will have a relationship. At this moment of discussion, a postulation is suggested:

MD tensile simulations performed at super-fast strain rates represent the nanoscale craze region in the macro-scale tensile specimen

as depicted in Figure 1(c). In other words, in the inhomogeneous plastic deformation scheme, the MD RUC describes not the macro specimen, but only the nanoscale craze region. Therefore, the relationship between the experimental strain rate $\dot{\epsilon}_{EXP}$ and the strain rate of the craze region $\dot{\epsilon}_{Craze}$ changes to the relationship between $\dot{\epsilon}_{EXP}$ and the MD strain rate $\dot{\epsilon}_{MD}$.

To uncover the relationship between the $\dot{\epsilon}_{EXP}$ and the $\dot{\epsilon}_{MD}$, a specific situation in which both the tensile experiment and the MD simulation describe simultaneously must be defined; the ductile-

brittle (DB) transition is employed as this specific situation. If the two s−s curves obtained from an MD simulation and an experiment are the ones at the DB transition at the same temperature, it can be asserted that the two different strain rates correspond to each other. In turn, while the macro specimen is stretched with the experimental strain rate $\dot{\epsilon}_{EXP}$, the nanoscale craze region is stretched with the MD strain rate $\dot{\epsilon}_{MD}$.

To this end, this thesis investigates the DB transition of a glassy polymer (PMMA) from both MD simulations and conventional tensile experiments. At a fixed temperature, tensile simulations and experiments are performed with different strain rates so that the strain rate at which the ductile behavior changes to the brittle behavior can be defined. By matching the results, the relationship between the MD strain rate and the experimental strain rate at the DB transition is discovered. Through this approach, it is confirmed that the application of MD simulations to the continuum scale should be restricted to the nano−scale region. Therefore, to obtain the atomistically−informed continuum description of a glassy polymer, a multi−scale continuum theory that can integrate and apply MD results

to the micro (or nano) scale must be employed.

In this thesis, the two-scale micromorphic theory is adopted where the macro-scale and the micro-scale possess independent stress-strain relationships. For the macro-scale, mechanical properties obtained from experiments are used while MD results are employed for the micro-scale. The two-scale micromorphic computation captured qualitatively the macroscopic response of glassy polymers when the ductile-brittle transition happens in the micro-scale. Furthermore, by adjusting length parameters in the formulation, it has been shown that a fully-compatible multi-scale simulation (both time-scale and length-scale) can be achieved, which implies the micromorphic theory can be employed as a physically reasonable multi-scale framework that can bridge molecular simulations and continuum computations.

1.3. Organization of the thesis

This thesis is organized in the following manner. In the next section, a literature review on multi-scale continuum theories is given according to two categories: hierarchical(section 2.1) and

concurrent(section 2.2) multi-scale method. Section 3 discusses the strain rate relationship between MD simulations and tensile experiments. Both simulation and experimental methods are given in section 3.1 and their results are in section 3.2. Through the discussion in section 3.3, the validity of using the multi-scale continuum models to elucidate the heterogeneous plastic deformation of glassy polymers is affirmed. In section 4, a step-wise description of the two-scale micromorphic theory is presented from the general overview of the micromorphic theory(section 4.1) to the adjusting MD results applicable to the finite element discretization(section 4.4). Results of micromorphic computations are discussed in Section 5, followed by salient conclusions and future works presented in Section 6.

2. Multi-scale continuum theories to incorporate nano-scale mechanics

2.1. Hierarchical coupling multi-scale model

Numerous attempts have been made to combine MD simulations with continuum theories. One of the most widely studied hierarchical multi-scale methods, the Cauch-Born rule (CBR) method, couples the atomistic and continuum models through a constant deformation gradient under the assumption of the affine deformation[24-26]. Recently, the coarse-grained Parinello-Rahman (CGPR) method, which is an extended form of the CBR method, has been developed to incorporate the inelastic deformation in an amorphous solid [27, 28]. It comprises material points representing respective atomistic RUC [27]. In each calculation step, a deformation gradient followed by a geometry optimization procedure shall be assigned to each material point in the RUC. The first Piola-Kirchhoff stress is calculated and applied to the respective material point in the continuum level. Then, new deformation gradients are designated and re-determined with the modified stresses. The CGPR approach is very stringent because there are physical reasons for every single

calculation. But since the atomic measurement is based on molecular mechanics, it is not possible to encompass the molecular dynamics and the deformation process in real-time domain.

2.2. Concurrent multi-scale model

The concurrent multi-scale model explicitly connects continuum and atomic modeling to continuum nodes by communicating nano-scale deformations. The microcontinuum field theories are rigorously-studied concurrent multi-scale approaches developed from the classical field theory in order to couple atomistic and continuum models. Micomorphic theory is considered to be the most successful, multi-scale, top-down model among different theories such as the Cosserat theory [29], couple stress theory [30], microstructure theory [31], micromorphic theory[32], and micropolar theory [33], the micomorphic theory is regarded as the most successful top-down multi-scale model [34]. The micromorphic theory introduced by Eringen in 1964 postulates that the material body is a continuous sequence of deformable particles with a finite size and inner structure that contradict the classic

hypothesis of the continuum in which material points have an infinite size and no internal structure. This was solved by Eringen, who substituted the deformable particle for a geometric point with several quantities of vectors. This is consistent with traditional continuum approaches in which physical properties such as vector and electric field are given for material points. Thus the micromorphic theory allows for different applications, including strain localization followed by Lüders bands in metals [35, 36] and phase transition of metals [37, 38].

Vernerey et al. expanded based on micromorphic theories [39, 40] to elucidate various deformation fields of porous and steel-alloys that possess two hard particle populations [41, 42]. The constitutive equation was then derived through the meso-domain homogenization method [43, 44]. A successful description of the micro deformation of steel alloy with two different micro-scales with respective plasticity was developed in the proposed multi-scale methodology. The new feature of the work is that the multi-scale continuum framework was created by in-house code and the ABAQUS UEL subroutine which consists of different stress-strain relationships at

each micro-scale. This thesis utilizes this two-scale micromorphic theory, which combines the MD tensile simulation findings and classical tensile experiments, to model glassy polymers that undergo inhomogeneous plastic deformation.

3. Strain rate relationship between nano- and macro-scale

3.1. Methods

3.1.1. Molecular dynamics (MD) modeling

The poly(methyl methacrylate) (PMMA) representative unit cell (RUC) was generated using the radical polymerization algorithm [16] where the initiation, propagation, and termination of the radical polymerization can be depicted. The model generation procedure is described below.

First, 6000 methacrylate (MMA) monomers and 60 phenyl radicals (initiators) described in the united-atom (UA) level are packed in an empty unit cell. The polymerization is initiated from phenyl radicals. Once initiators are activated, all close-contacts between the radicals and reactive sites in monomers are calculated. If the distance of a close-contact is shorter than the cutoff radius (varies from 7Å to 11Å), a bond is generated between the radical and the reactive site in the monomer, followed by a radical shift from the initial position to the terminal backbone atom of the chain. The RUC then goes through the geometry optimization and a short NVT

ensemble for 2000 steps. This process is repeated until the desired degree of polymerization is reached. In this thesis, at the end of the polymerization, the PMMA RUC reached the number average molecular weight of 9,587 (g/mol) and weight average molecular weight of 13,961 (g/mol) in a ($100 Å \times 100 Å \times 100 Å$) box. The RUC consisted of 40260 united atoms and the PBC was introduced to avoid the surface effect.

The UA level molecular dynamics simulations were performed on the largescale atomic/molecular massively parallel simulator (LAMMPS) [45]. The combined PCFF-TraPPE (UA) force field specially designed for the radical polymerization of PMMA was employed [16]. In short, for bonded potentials, only valence terms (bond, angle, dihedral, and out-of-plane) in the conventional PCFF force field were used while the TraPPE(UA) force field was employed for the non-bonded potentials where the non-bonded parameters are listed in Table 1. The Lorentz-Berthelot mixing rule was used for the non-bonded potential between different kinds of united atoms.

An annealing simulation was performed to equilibrate the RUC

grown by the polymerization algorithm: NVT (same number of atoms, constant volume, and temperature) ensemble simulation for 0.2 ns from 600K to 300K followed by NPT (same number of atoms, constant pressure and temperature) ensemble simulation for 0.5 ns at 300K and 1 atm. The Nose–Hoover thermostat and barostat were employed for the whole ensemble simulations [46]. The OVITO program was employed for visualization [47].

Dynamic tensile simulations were conducted following the description in our group's previous paper [5]. The RUC was stretched in x−direction with a constant strain rate ($\dot{\varepsilon}_{MD}$) while the other two directions were managed by the Nose−Hoover barostat.

Table 1 Non-bonded parameters of the TraPPE (UA) force field [16]. Corresponding force field types in PCFF are listed in the second column.

TraPPE (UA)	PCFF	σ ($\AA$)	ϵ [$Kcal/mol$]	Charge (e^-)
C(aro)	cp	3.88	0.042	0
C(sp2)	c=1	3.85	0.044	0
C(sp3)	c	3.5	0.066	0
C(carbonyl)	c_1	3.82	0.079	0.4
CH(sp2)	cp	3.71	0.103	0
CH(sp3)	c1	4.68	0.020	0
CH2(sp2)	c=	3.675	0.169	0
CH2(sp3)	c2	3.95	0.091	0
CH3(sp3)	c3	3.75	0.195	0
CH3(ether)	c3	3.75	0.195	0.25
O(ether)	o_2	2.8	0.109	−0.25

3.1.2. Tensile experiments for PMMA dog-bone specimens

PMMA specimens used in this thesis are commercial samples purchased from Korea Polymer. The dimension of the specimen is the Type 1 sample of the ASTM D638 standard test method as illustrated in Figure 2(a). A tensile machine (QUASAR 5, Galdabini, Italy) was employed to carry out tensile tests at various strain rates ranging from 0.1~200 mm/min while the temperature was controlled by a heating/cooling chamber. A picture taken during the tensile test is shown in Figure 2(b). Various temperatures (298 K, 308K, 318K, 328K, 338K) were investigated for the tensile tests.

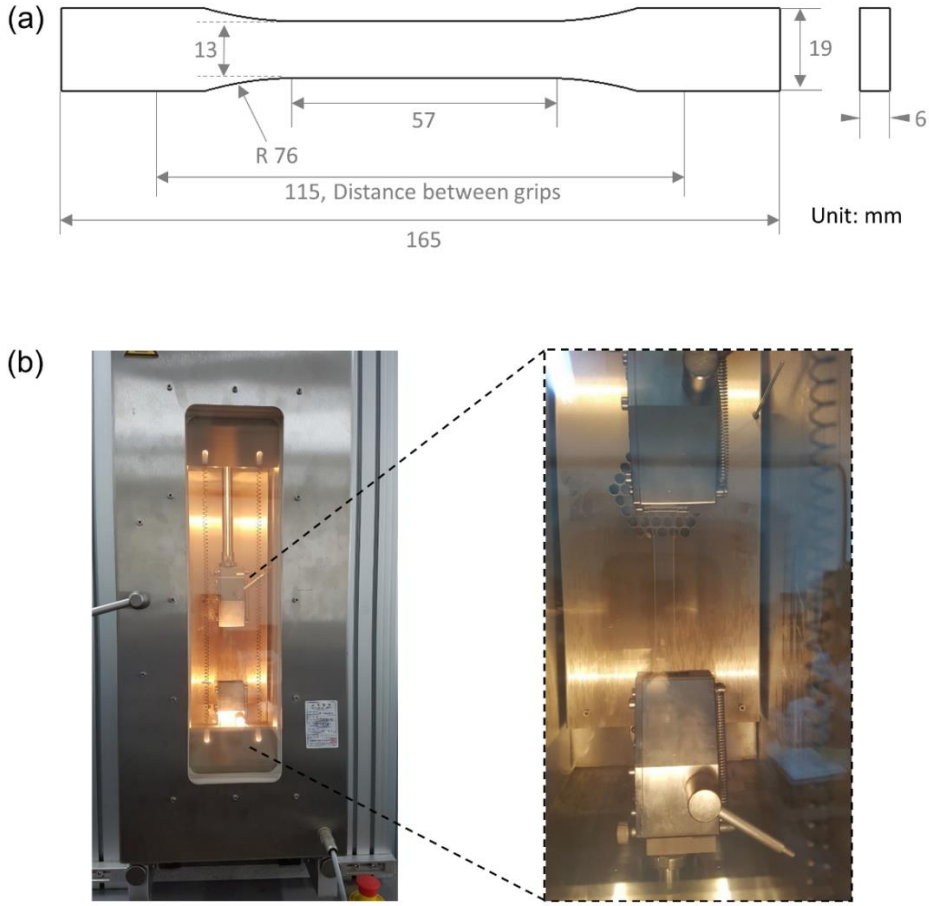

Figure 2 Diagrams of tensile experiments. (a) Type 1 specimen of the ASTM D638 standard test method. (b) A picture taken during the tensile test.

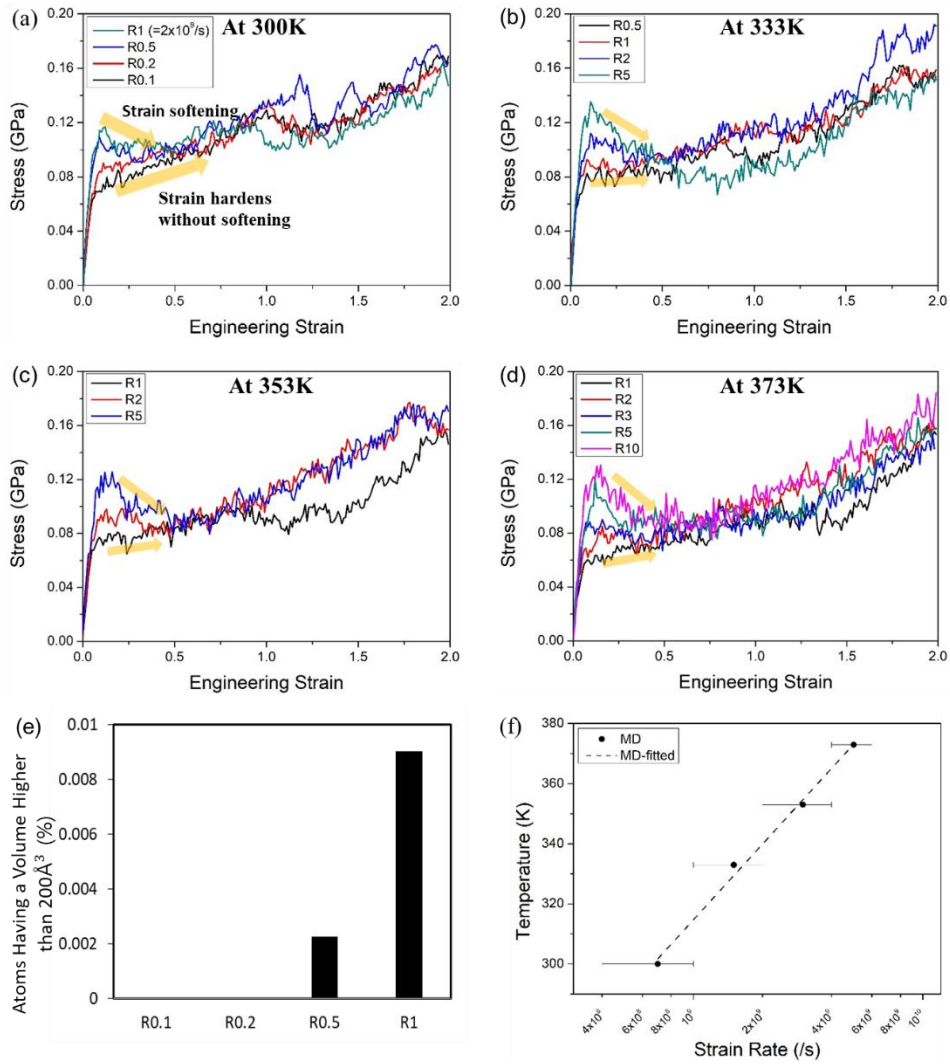

Figure 3 DB transition of PMMA observed in both MD simulations. MD s-s curves at (a) 300K, (b) 333K, (c) 353K, and (d) 373K. (e) Atoms having volumes higher than **200Å** at engineering strain of 1.0 in case of tensile simulations at 300K. The counts are expressed in number percentage. (f) DB transition curve in MD simulations with a logarithmic fit.

3.2. Ductile-brittle transition results

3.2.1. MD simulation results

At 300K, large deformational tensile tests were performed on a PMMA RUC at various strain rates ranging from R0.1 to R1 (relative units, R1 corresponds to 2×10^9/s while R0.1 corresponds to 2×10^8/s). The corresponding s-s curves are plotted in Figure 3(a). Curves in Figure 3(a) show a clear dependence of the yield stress on the strain rate. The yield stress increases as the strain rate increases, which is commonly observed from experiments and simulations [11, 22]. After the yield point, the curves show two different behavior; at high strain rates (R0.5 and R1), the strain softening occurs after the yield point whereas the material hardens without softening at low strain rates (R0.1 and R0.2). As mentioned before, the softening, occurring at high strain rates, is due to the craze initiation and void formation which has also been reported in the literature [19, 20]. In Figure 4, a clear void is observed at R1 (a, b) whereas no outstanding void can be detected at R0.1 (c, d). At low strain rate, the material hardens after the yield point without showing any strain softening. The low strain rate provides enough relaxation time to

polymer chains so that they are stretched without creating any void or crazing as can be seen in Figure 4 (c,d). At this strain rate, the shear banding is the major deformation mechanism of the material rather than the crazing. Therefore, from Figure 3(a), one can conclude that the DB transition at 300K takes place at strain rate from R0.2 to R0.5.

It can also be specified from the atomic volume analysis, which yields the same result. From tensile simulations at 300K, the atomic volume was calculated quantitatively through the Voronoi tessellation, [5, 48] and atoms having high atomic volumes (higher than $200\,\text{Å}$) were counted. Note that the atomic volume was captured at engineering strain of 1.0 since it is in the middle of the craze growth. The result is plotted in Figure 3(e). At R0.1 and R0.2, there are no atoms having atomic volume higher than $200\,\text{Å}$. Starting from R0.5, however, there exists atoms having an extremely high volume. Therefore, the ductile-brittle transition strain rate can be defined as R0.2 to R0.5 ($4\times10^{8}/s \sim 10^{9}/s$), which is the same as the one obtained from MD s-s curves at 300K.

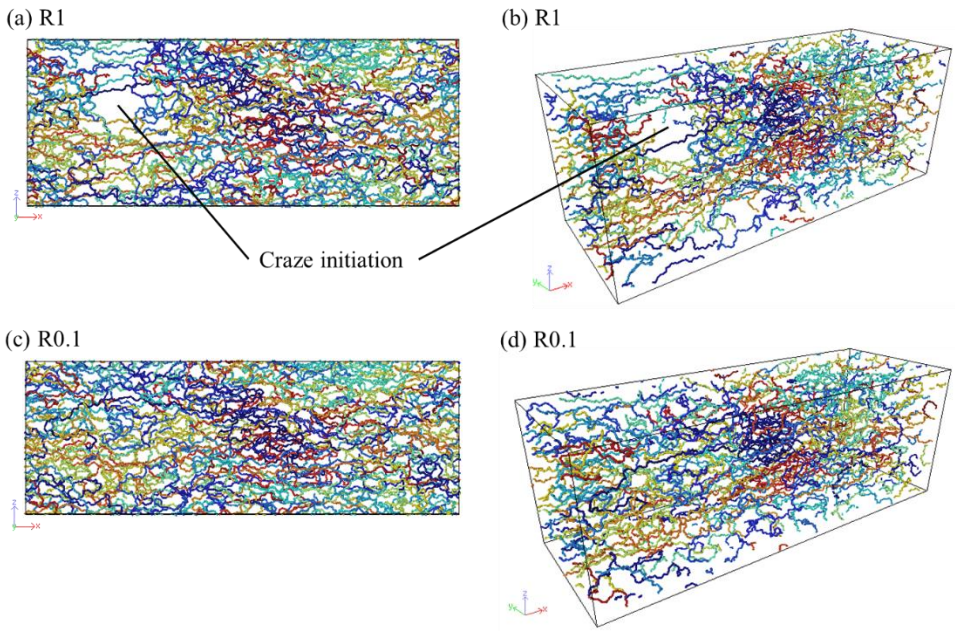

Figure 4 Snapshots of tensile simulations at 300K and 1.0 engineering strain. Strain rate: (a,b) are R1, (c,d) are R0.1. Polymer chains are colored differently, chain by chain.

The same tensile simulation was carried out at 333K, 353K, and 373K (Figure 3(b–d)). Using the same criteria discussed at 300K, the DB transition strain rate was captured at each temperature. The final result is illustrated in Figure 3(f) with a logarithmic fit expressed as:

$$T_{MD} = 36.326\, ln\, \dot{\epsilon}_{MD}^{DB} - 438.08 \qquad (1)$$

where T_{MD} is the temperature and $\dot{\epsilon}_{MD}^{DB}$ is the MD strain rate at the DB transition. The transition strain rate increases as the temperature

increases because glassy polymers become ductile at high temperatures. Thus, the DB transition curve obtained from current MD simulations exhibits a general phenomenon of the DB transition.

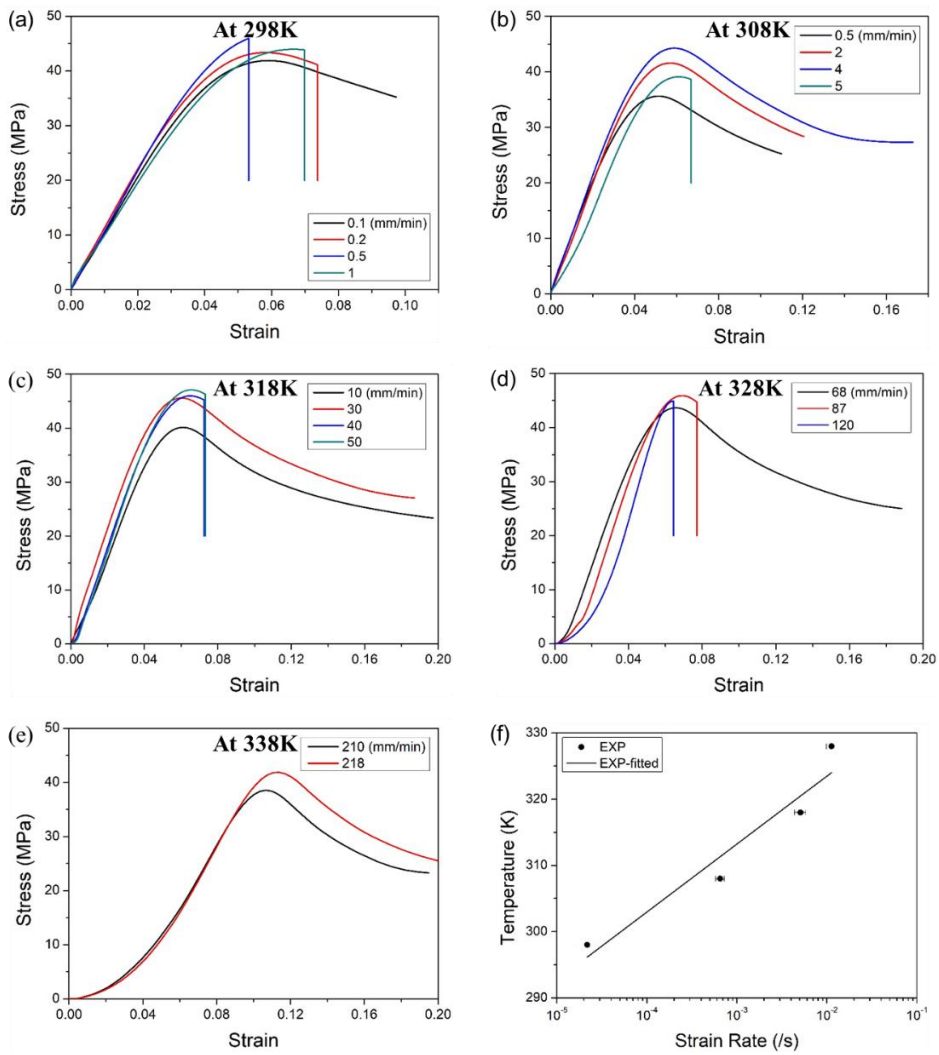

Figure 5 DB transition of PMMA observed in tensile experiments. S-s curves at (a) 298K, (b) 308K, (c) 318K, (d) 328K, and (e) 333K. (f) DB transition curve in tensile experiments with a logarithmic fit.

3.2.2. Tensile experimental results

Figure 5(a) is experimental s-s curves at 298K and various strain rates. PMMA is ductile at 0.1mm/min while it is brittle at strain rates higher than 0.2mm/min. Thus, the DB transition takes place between 0.1 and 0.2mm/min. Considering that the distance between grips is 115mm, the transition strain rates in per second unit (/s) are 1.45×10^{-5}/s and 2.90×10^{-5}/s, which are plotted in Figure 5(f). These two values are both ends of the error bar while the mid-point was marked by a circle dot. The same experiment was performed at 308K, 318K, and 328K as can be seen in Figure 5(b-e), and the transition strain rates at each temperature are also plotted in Figure 5(f). The logarithmic fit in Figure 5(f) is written in Eq.(2):

$$T_{EXP} = 4.4589 \, ln \, \dot{\epsilon}_{EXP}^{DB} + 344.04. \quad (2)$$

Similar to the Eq.(1), the DB transition strain rate increases as the temperature increases.

3.3. Discussions for the strain rate relationship

Following our postulation, at the same temperature, the DB transition strain rates in MD simulations and the experiments can be matched by making T_{MD} and T_{EXP} in Eq. (1) and Eq.(2) equal:

$$\dot{\epsilon}_{EXP}^{DB} = \mathrm{e}^{-175.41} \cdot (\dot{\epsilon}_{MD}^{DB})^{8.1469}. \quad (3)$$

Eq.(3) connects the MD strain rate $\dot{\epsilon}_{MD}^{DB}$ and the experimental strain rate $\dot{\epsilon}_{EXP}^{DB}$ at the DB transition. For instance, the experimental strain rate corresponding to the MD strain rate R1 is 0.39 /s at the DB transition. The two DB transition graphs in Figure 3(f) and Figure 5(f) are then co-plotted in Figure 6 by employing Eq.(3). The two fitted lines coincide because both ends of the two x-axes are matched according to Eq.(3). The strain rate discrepancy between MD and experimental strain rates in Figure 6 and Eq.(3) was induced by the inhomogeneous plastic deformation. However, the gap between $\dot{\epsilon}_{MD}^{DB}$ and $\dot{\epsilon}_{EXP}^{DB}$ decreases as the temperature increases from room temperature. Thus the point at which the two strain rates become the same ($\dot{\epsilon}_{MD}^{DB} = \dot{\epsilon}_{EXP}^{DB}$) is calculated. The strain rate and the temperature at this point is 4.56×10^{10}/s and 180.36℃, respectively, where the temperature is slightly above the melting temperature of

PMMA, known as 160℃. This result means that if the PMMA melts, the MD strain rate becomes equal to the experimental strain rate.

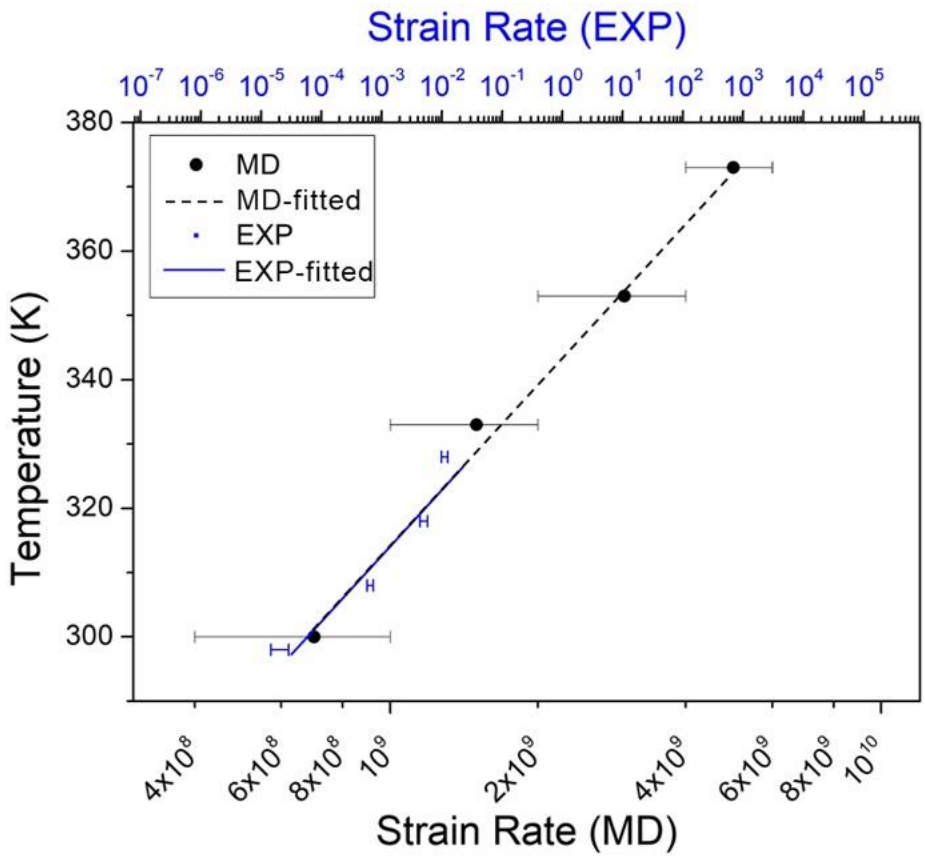

Figure 6 The final DB transition curve in which the MD result and the experimental result are co-plotted. The error bar denotes the range of the DB transition strain rate and the median value is selected as a representative value.

As mentioned before, the reason why strain rates of the macroscale and the nanoscale are different is due to this inhomogeneous deformation scheme. However, as the polymer melts,

it no longer deforms heterogeneously because it flows. Therefore, at this temperature, it can be considered as a homogeneous deformation so that the $\dot{\epsilon}_{MD}^{DB}$ and the $\dot{\epsilon}_{EXP}^{DB}$ becomes the same. This result tells that the assumption of homogeneous deformation under the PBC condition only holds at high temperature where the polymer is in the liquid state. When the polymer is in the solid state, on the other hand, the inhomogeneous deformation scheme must be considered. To discuss these results profoundly, it is necessary to start the discussion from the original works of MD simulations for polymers.

MD simulations for polymers were initiated with an investigation on the dynamics of polymer melts, particularly, for the non-entangled polymer melt ($N < N_e$, entanglement length) whose dynamic behavior coincides with the theoretic prediction of Rouse model [49, 50]. Then, entangled polymer networks ($N > N_e$) utilizing the coarse-grained method were studied [51, 52]. These entangled polymer melts were employed to unveil the crossover from Rouse to reptation mode where they successfully predicted the transition of the self-diffusion coefficient and the zero-shear rate viscosity as the chain length increases [53].

By virtue of progress in computational power and atomistic expression of the virial stress, MD simulations for polymer melts were followed by mechanical tensile/compression simulations for glassy polymers containing long chains, and investigations on their stress–strain relationships [45]. However, the dynamic tensile simulations have an intrinsic limitation that they are conducted at super–fast strain rates [54–56]. Nevertheless, numerous researches that calculate mechanical properties or characterize yield criteria of bulk polymers using MD simulations have been reported [11, 15].

The result in the current thesis offers conclusive evidence on the reason why MD simulations for polymer melts have successfully predicted the theoretic models (Rouse and reptation model) whereas those for glassy polymers have not fully overcome the limitation of super–fast strain rates. Since the homogeneous deformation assumption is available for polymer melts, reasonable atomic models can be achieved even in relatively small length scales when it is combined with the PBC. On the other hand, glassy polymers deform heterogeneously while MD simulations with super–fast strain rates

are able to describe only limited nanoscale regions. Therefore, a single MD RUC for glassy polymers never succeed to depict bulk deformation phenomena. Hence, future MD tensile simulations on glassy polymers should focus on the inhomogeneous plastic deformation scheme and break down with various length scales dealing with different deformation mechanisms. Toward this, it is expected that the relationship between MD and experimental strain rates in Eq.(3) can be extensively utilized since it serves as a yardstick when estimating strain rates of local deformation regions.

In short, the following postulation has been suggested:

MD tensile simulations performed at super-fast strain rates represent the nanoscale craze region in the macro-scale tensile specimen.

The correspondence of the MD strain rate $\dot{\epsilon}_{MD}^{DB}$ and the experimental strain rate $\dot{\epsilon}_{EXP}^{DB}$ at the DB transition successfully predicted the melting point of PMMA at which the homogeneous and the inhomogeneous deformation scheme diverge. Therefore, it is concluded that the suggested postulation is reasonable. The implication of this result is as follows. First, numerous MD tensile

simulations for glassy polymers conducted under the homogeneous deformation scheme should be re-examined, especially those that consider the plastic regime. It is inaccurate to assume that the MD RUC represents the whole macro specimen when it is in the plastic regime. Second, to understand the constitutive relation of a glassy polymer by using the MD simulation, a multi-scale continuum approach must be employed which can incorporate MD results as the physics of the micro (or nano) scale. The micromorphic theory was adopted as a powerful multi-scale approach for this purpose [41, 42, 57] in which constitutive relations in various microscales can be incorporated.

4. Multi-scale micromorphic theory

4.1. General overview of the micromorphic theory

Compared to traditional continuum mechanics, the main difference in micromorphic theory is that any material point in the macro scale is the origin of micro-scale, where independent stress-strain relations are applied. Microscale existence allows multiscale physics to be included in the theory of continuum. Figure 7 is a general diagram of the two-scale micromorphic theory. The macro-scale Ω has x_1 and x_2 coordinate system while the micro-scale Ω^m originated from point $\mathbf{x}$ is expressed by x_1^m and x_2^m coordinate system with the characteristic length l^m. Note that the superscript 'm' reveals the micro-scale in this thesis. The micro-velocity $\mathbf{v}^m$ is given as:

$$\mathbf{v}^m = \mathbf{v}^m(\mathbf{x} + \mathbf{x}^m). \tag{4}$$

By Taylor series expansion with the first term truncation, it is expressed with the micro-velocity gradient $\mathbf{L}^m(\mathbf{x})$:

$$\mathbf{v}^m = \mathbf{v}^m(\mathbf{x}) + \mathbf{L}^m(\mathbf{x}) \cdot \mathbf{x}^m. \tag{5}$$

Therefore, the velocity gradient of the micro-scale is described as a

function of the macro−scale coordinate $\mathbf{x}$ as:

$$\mathbf{L}^m(\mathbf{x}) = \frac{\partial \mathbf{v}^m}{\partial \mathbf{x}^m} \tag{6}$$

where $\mathbf{v}^m(\mathbf{x}) = 0$ by definition. The micro−scale velocity gradient represents the micro−scale kinematics since it is an independent variable. Same as the macroscopic velocity $\mathbf{v}$, the microscopic velocity gradient $\mathbf{L}^m$ is the kinematics variable assigned to the material points.

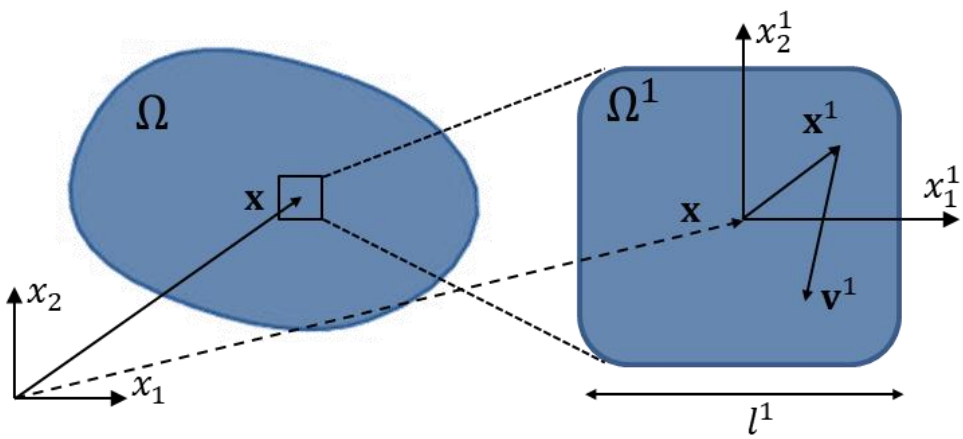

Figure 7. General diagram of the two-scale micromorphic theory.

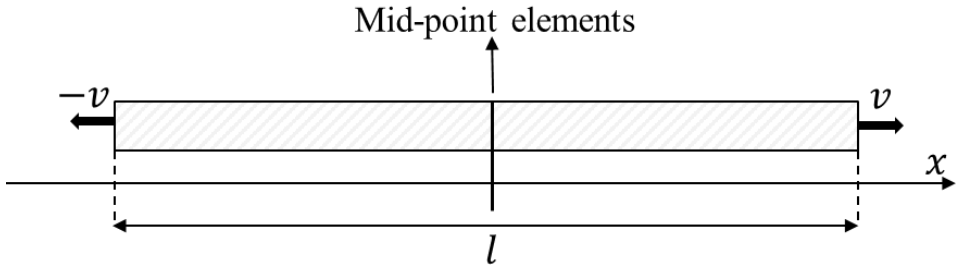

Figure 8. Schematic illustration of the one-dimensional example of the micromorphic theory.

4.2. Two-scale micromorphic theory

In this thesis, only the one-dimensional example shown at Figure 8 is going to be dealt with where the two ends of the bar specimen are lengthened with a constant speed(v) and the macro yield stress of the center of the bar are reduced by 10%. This describes a one-dimensional tensile specimen, the midpoint of which is weak. The weak element of the midpoint is the nanoscale defect when it has a low density of molecular entanglement or micro-inclusions locally. Many MD studies have shown that the crazing and local plastic zone begins in this region [19, 20, 58]. The post-yield behavior, therefore, starts in these mid-point elements first. With this one-dimensional model, the micromorphic theory is used to combine MD simulation results and experimental results.

$$\delta P_{int} + \delta P_{kin} - \delta P_{ext} = 0 \qquad (7)$$

Eq. (7) shows the principle of virtual power for the two-scale micromorphic theory. Both δP_{kin} and δP_{ext} are neglected as the one-dimensional example does not have both kinetic and external virtual power. From the internal virtual power (δP_{int}) in the micromorphic model developed by Vernerey et al. [41], the one-dimensional governing equation is written as Eq. (8)

$$\delta P_{int} = \int_{\Omega} \left[\boldsymbol{\sigma} : \delta \mathbf{L} + \bar{\boldsymbol{\sigma}}^{m} : \left(\delta \mathbf{L}^{m} - \delta \mathbf{L} \right) + \bar{\bar{\boldsymbol{\sigma}}}^{m} \vdots \nabla \left(\delta \mathbf{L}^{m} \right) \right] \mathrm{d}\Omega \qquad (8)$$

where $\boldsymbol{\sigma}$, $\bar{\boldsymbol{\sigma}}^{m}$,and $\bar{\bar{\boldsymbol{\sigma}}}^{m}$ are the macro-stress, the micro-stress, and the micro-stress couple, respectively. The conventional spatial average of macroscopic force per unit area, the macro-stress $\boldsymbol{\sigma}$, is given with the macro-scale virtual velocity gradient $\delta \mathbf{L}$ as work conjugate. The micro-stresses $\bar{\boldsymbol{\sigma}}^{m}$, $\bar{\bar{\boldsymbol{\sigma}}}^{m}$ are the spatial average of microscopic forces due to the inhomogeneous deformation of microstructures [41]. The stress redistribution occurs on the length of the micro-domain according to these micro stresses. The couple stress $\bar{\bar{\boldsymbol{\sigma}}}^{m}$ means the spatial average of the microscopic moment.

The micro-stress and the couple stress are linked to $\delta \mathbf{L}^m - \delta \mathbf{L}$ and $\nabla(\delta \mathbf{L}^m)$ as work conjugates, where $\mathbf{L}^m$ is the velocity gradient of the micro-scale and $\nabla \mathbf{L}^m$ is the gradient of $\mathbf{L}^{\mathrm{m}}$ [41].

The strong form of the governing equation is derived by integrating Eq. (8) by part and applying the divergence theorem:

$$\begin{aligned} \delta P_{int} = -\int_{\Omega} \left[\{\nabla \cdot (\boldsymbol{\sigma} - \overline{\boldsymbol{\sigma}}^m)\} \cdot \delta \boldsymbol{v} + \{\nabla \cdot \overline{\overline{\boldsymbol{\sigma}}}^m - \overline{\boldsymbol{\sigma}}^m\} : \delta \mathbf{L}^m\right] \mathrm{d}\Omega \\ + \int_{\Gamma} \left[\{(\boldsymbol{\sigma} - \overline{\boldsymbol{\sigma}}^m) \cdot \boldsymbol{n}\} \cdot \delta \boldsymbol{v} + \{\overline{\overline{\boldsymbol{\sigma}}}^m \cdot \boldsymbol{n}\} : \delta \mathbf{L}^m\right] \mathrm{d}\Gamma . \end{aligned} \tag{9}$$

The virtual internal power consists of integrals over the macro-domain Ω and the boundary Γ. Therefore, the governing equation is written in the strong form as:

$$\nabla \cdot (\boldsymbol{\sigma} - \overline{\boldsymbol{\sigma}}^m) = 0 \; and \; \nabla \cdot \overline{\overline{\boldsymbol{\sigma}}}^m - \overline{\boldsymbol{\sigma}}^m = 0 \; in \; \Omega \tag{10}$$

with boundary conditions:

$$(\boldsymbol{\sigma} - \overline{\boldsymbol{\sigma}}^m) \cdot \boldsymbol{n} = 0 \; and \; \overline{\overline{\boldsymbol{\sigma}}}^m \cdot \boldsymbol{n} = 0 \; at \; \Gamma . \tag{11}$$

The first equation in Eq. (10) is the macroscopic static equilibrium equation in which the Cauchy stress is adjusted with additional micro-stress contribution. The second equation of Eq. (10) is the balance equation of the micro-scale momentum. Without question, with the homogeneous assumption of deformation where

microstresses are ignored, Eq. (10) returns the standard static equation known as $\nabla \cdot \boldsymbol{\sigma} = 0$.

4.3. Constitutive relationship

The Cauchy stress and the velocity gradient should be replaced with generalized forms to obtain the constitutive relationship. The generalized stress vector $\boldsymbol{\Sigma}$ and the generalized rate of deformation $\boldsymbol{\Delta}$ is given as:

$$\boldsymbol{\Sigma} = \begin{bmatrix} \boldsymbol{\sigma} \\ \bar{\boldsymbol{\sigma}}^{m} \\ \bar{\bar{\boldsymbol{\sigma}}}^{m} \end{bmatrix}, \ \boldsymbol{\Delta} = \begin{bmatrix} \mathbf{L} \\ \mathbf{L}^{m} - \mathbf{L} \\ \nabla \mathbf{L}^{\mathrm{m}} \end{bmatrix}. \tag{12}$$

To encompass large deformation, objective rates need to be employed. In this thesis, the Jaumann stress rate expressed as eq (13) is adopted

$$\boldsymbol{\Sigma}^{\nabla} = \begin{bmatrix} \sigma_{ij}^{\nabla} \\ \bar{\sigma}_{ij}^{m\nabla} \\ \bar{\bar{\sigma}}_{ijk}^{\mathrm{m}\nabla} \end{bmatrix} \tag{13}$$

where each component of the Jaumann rate is divided into two parts: material time derivative and rotational part,

$$\sigma_{ij}^{\nabla} = \dot{\sigma}_{ij} - (\sigma_{kj}W_{ik} + \sigma_{ik}W_{jk})$$

$$\bar{\sigma}_{ij}^{m\nabla} = \dot{\bar{\sigma}}_{ij}^{m} - (\bar{\sigma}_{kj}^{m}W_{ik} + \bar{\sigma}_{ik}^{m}W_{jk}) \qquad (14)$$

$$\bar{\bar{\sigma}}_{ijk}^{m\nabla} = \dot{\bar{\bar{\sigma}}}_{ijk}^{m} - (\bar{\bar{\sigma}}_{ljk}^{m}W_{il} + \bar{\bar{\sigma}}_{ilk}^{m}W_{jl} + \bar{\bar{\sigma}}_{ijl}^{m}W_{kl}).$$

The rotation tensor $\mathbf{W}$ equals to zero in this thesis since the irrotational deformation is assumed in the one-dimensional example.

The generalized rate of deformation is divided into two parts: elastic and plastic part.

$$\boldsymbol{\Delta} = \boldsymbol{\Delta}^{\mathrm{e}} + \boldsymbol{\Delta}^{\mathrm{p}}. \qquad (15)$$

Finally, the constitutive relationship in the elastic regime is given as:

$$\begin{bmatrix} \boldsymbol{\sigma} \\ \bar{\boldsymbol{\sigma}}^{m} \\ \bar{\bar{\boldsymbol{\sigma}}}^{m} \end{bmatrix}^{\nabla} = \begin{bmatrix} \bar{\mathbf{C}} & 0 & 0 \\ 0 & \bar{\mathbf{C}}^{m} & \bar{\mathbf{B}}^{m} \\ 0 & \bar{\mathbf{B}}^{m} & \bar{\bar{\mathbf{C}}}^{m} \end{bmatrix} \cdot \begin{bmatrix} \mathbf{L} \\ \mathbf{L}^{m} - \mathbf{L} \\ \nabla\mathbf{L}^{m} \end{bmatrix}^{e}. \qquad (16)$$

The first term on the right side of Eq.(16) is denoted as the tangent stiffness matrix $\mathbf{C}$:

$$\mathbf{C} = \begin{bmatrix} \bar{\mathbf{C}} & 0 & 0 \\ 0 & \bar{\mathbf{C}}^{m} & \bar{\mathbf{B}}^{m} \\ 0 & \bar{\mathbf{B}}^{m} & \bar{\bar{\mathbf{C}}}^{m} \end{bmatrix} \qquad (17)$$

where $\bar{\mathbf{C}}$ is the macroscopic elastic matrix and it is equal to the Young's modulus of the macro-scale in case of the one-dimensional example. $\bar{\mathbf{C}}^{m}$, $\bar{\mathbf{B}}^{m}$, and $\bar{\bar{\mathbf{C}}}^{m}$ are elastic matrices relating the micro

velocity gradients ($\mathbf{L}^m - \mathbf{L}$ and $\nabla\mathbf{L}^m$) to the micro stress rates ($\bar{\boldsymbol{\sigma}}^{m\nabla}$ and $\bar{\bar{\boldsymbol{\sigma}}}^{m\nabla}$), which occurs from the heterogeneous deformation scheme.

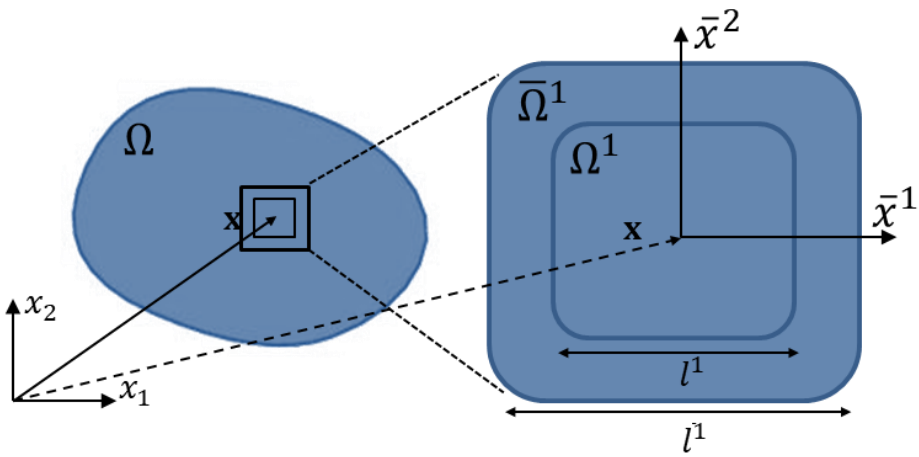

Figure 9. Schematic diagram of the averaging operation for the calculation of elastic matrices. $\boldsymbol{\Omega}$, $\boldsymbol{\Omega}^m$, and $\bar{\boldsymbol{\Omega}}^m$ with the corresponding length scale $\boldsymbol{l}$, $\boldsymbol{l}^m$, and $\bar{\boldsymbol{l}}^m$ refers to the macro-scale, micro-scale, and meso-scale, respectively.

Elastic matrices can be calculated from the averaging operation introduced by Vernerey et al. [41, 42]. At first, a meso-scale ($\overline{\Omega}^{\mathrm{m}}$) is introduced which is associated with the micro-scale and centered at point $\mathbf{x}$ as shown in Figure 9. The size of the meso-scale ($\bar{l}^m$) is defined as the region wherein the micro-velocity gradient $\mathbf{L}^m$ varies linearly. In this thesis, it is set as $\bar{l}^m = 2l^m$ for simplicity [41]. The inhomogeneous strain field inside the meso-scale $\boldsymbol{\sigma}^m$ and its power conjugate $\mathbf{L}^{\mathrm{m}} - \mathbf{L}$ is then defined. Next, by definition, the virtual

internal power density at point $\mathbf{x}$ is given as an average of the virtual power over the meso-volume $\overline{\Omega}^m$ as follows:

$$\delta p(\mathbf{x}) = \boldsymbol{\sigma}: \delta \mathbf{L} + \frac{1}{\overline{\Omega}^m} \int_{\overline{\Omega}^m} \boldsymbol{\sigma}^m : \left(\delta \mathbf{L}^m - \delta \mathbf{L} \right) \mathrm{d}\overline{\Omega}^m . \tag{18}$$

In the meso-scale, the Taylor series expansion on the velocity gradient $\mathbf{L}^m$ returns:

$$\mathbf{L}^m(\mathbf{x} + \bar{\mathbf{x}}^m) = \mathbf{L}^{\mathrm{m}}(\mathbf{x}) + \nabla \mathbf{L}^m \cdot \bar{\mathbf{x}}^m \tag{19}$$

where the meso-scale is expressed with $\bar{\mathbf{x}}^m$ coordinate system. By substituting Eq.(19) to Eq.(18) and comparing with the internal virtual power in Eq.(8), the homogenized micro stress $\bar{\boldsymbol{\sigma}}^m$ and the micro stress couple $\bar{\bar{\boldsymbol{\sigma}}}^m$ is written with $\boldsymbol{\sigma}^m$ as:

$$\begin{aligned} \bar{\boldsymbol{\sigma}}^m &= \frac{1}{\overline{\Omega}^m} \int_{\overline{\Omega}^m} \boldsymbol{\sigma}^m(\mathbf{x} + \bar{\mathbf{x}}^m) \, \mathrm{d}\overline{\Omega}^m \\ \bar{\bar{\boldsymbol{\sigma}}}^m &= \frac{1}{\bar{\Omega}^m} \int_{\overline{\Omega}^m} \boldsymbol{\sigma}^m(\mathbf{x} + \bar{\mathbf{x}}^m) \otimes \bar{\mathbf{x}}^m \, \mathrm{d}\overline{\Omega}^m . \end{aligned} \tag{20}$$

Now, it is assumed that the stress rate $\boldsymbol{\sigma}^{m\nabla}$ and the relative micro-velocity gradient $\mathbf{L}^m - \mathbf{L}$ have a linear relationship with a constant of the micro-scale elastic matrix $\mathbf{C}^m$ as follows:

$$\boldsymbol{\sigma}^{m\nabla}(\mathbf{x} + \bar{\mathbf{x}}^m) = \mathbf{C}^m : [\mathbf{L}^m(\mathbf{x} + \bar{\mathbf{x}}^m) - \mathbf{L}(\mathbf{x})]. \tag{21}$$

Substituting Eq.(21) into Eq.(20) yields the following equations:

$$\bar{\boldsymbol{\sigma}}^m = \frac{1}{\bar{\Omega}^m} \int_{\bar{\Omega}^m} \mathbf{C}^{\mathrm{m}} : [\mathbf{L}^m(\mathbf{x} + \bar{\mathbf{x}}^m) - \mathbf{L}(\mathbf{x})] \, \mathrm{d}\bar{\Omega}^m$$

$$\bar{\bar{\boldsymbol{\sigma}}}^m = \frac{1}{\bar{\Omega}^m} \int_{\bar{\Omega}^m} \mathbf{C}^{\boldsymbol{m}} : [\mathbf{L}^m(\mathbf{x} + \bar{\mathbf{x}}^m) - \mathbf{L}(\mathbf{x})] \otimes \bar{\mathbf{x}}^m \, \mathrm{d}\bar{\Omega}^m . \tag{22}$$

Finally, by comparing Eq.(22) with the constitutive relationship in Eq.(16), the homogenized elastic matrices $\bar{\mathbf{C}}^m$, $\bar{\mathbf{B}}^m$, and $\bar{\bar{\mathbf{C}}}^m$ are determined as follows:

$$\bar{\mathbf{C}}^m = \frac{1}{\bar{\Omega}^m} \int_{\bar{\Omega}^m} \mathbf{C}^m \, \mathrm{d}\bar{\Omega}^m$$

$$\bar{\mathbf{B}}^m = \frac{1}{\bar{\Omega}^m} \int_{\bar{\Omega}^m} \mathbf{C}^m \otimes \bar{\mathbf{x}}^m \, \mathrm{d}\bar{\Omega}^m \tag{23}$$

$$\bar{\bar{\mathbf{C}}}^m = \frac{1}{\bar{\Omega}^m} \int_{\bar{\Omega}^m} \mathbf{C}^m \otimes \bar{\mathbf{x}}^m \otimes \bar{\mathbf{x}}^m \, \mathrm{d}\bar{\Omega}^m .$$

In case of one-dimensional example, the averaged quantities are given as:

$$\bar{\mathbf{C}}^m = \frac{1}{\bar{l}^m}\int_{-\bar{l}^m/2}^{\bar{l}^m/2} \mathbf{C}^m \, \mathrm{d}\bar{x}^m = \mathbf{C}^m$$

$$\bar{\mathbf{B}}^m = \frac{1}{\bar{l}^m}\int_{-\bar{l}^m/2}^{\bar{l}^m/2} \mathbf{C}^m \bar{x}^m \, \mathrm{d}\bar{x}^m = 0 \qquad (24)$$

$$\bar{\bar{\mathbf{C}}}^m = \frac{1}{\bar{l}^m}\int_{-\bar{l}^m/2}^{\bar{l}^m/2} \mathbf{C}^m (\bar{x}^{\mathrm{m}})^2 \, \mathrm{d}\bar{x}^m = \mathbf{C}^m \frac{\left(\bar{l}^m\right)^2}{12}.$$

In the plastic regime, the macro-scale is assigned with the perfect plasticity to let the micro-scale predominant when the macro yield occurs [42]. Thus the yield criterion of the macro-scale is expressed as:

$$\Phi(\sigma) = |\sigma| - \sigma_y \qquad (25)$$

where $|\sigma|$ and σ_y are effective stress and the macro-scale yield stress, respectively. In case of the one-dimensional example, the effective stress is equal to the macro-scale Cauchy stress.

The micro-scale can take both perfect plasticity and isotropic hardening plasticity. From linear s-s curves of MD tensile simulations, the plasticity of the micro-scale is selected. Since the plasticity varies with various s-s curves of different strain rates in MD simulations, a yield criterion based on the

critical yield strain is convenient. Therefore, for the micro-scale, the critical yield strain is employed for the yielding criteria.

4.4. Finite element discretization

The next step is the finite element discretization. A one-dimensional two-node element with an elemental variable $\mathbf{d}^{\mathbf{e}}$ is used

$$\mathbf{d}^{\mathbf{e}} = \begin{bmatrix} v_1 \\ L_1^m \\ v_2 \\ L_2^m \end{bmatrix} \tag{26}$$

where the subscript (1, 2) refers to the elemental node number. The generalized strain rate ($\boldsymbol{\Delta}$) can be written with the matrix Q (similar to the shape function derivative):

$$\boldsymbol{\Delta} = \mathbf{Q}\mathbf{d}^{\mathbf{e}} = \begin{bmatrix} \frac{\partial N_1}{dx} & 0 & \frac{\partial N_2}{dx} & 0 \\ -\frac{\partial N_1}{dx} & N_1 & -\frac{\partial N_2}{dx} & N_2 \\ 0 & \frac{\partial N_1}{dx} & 0 & \frac{\partial N_2}{dx} \end{bmatrix} \cdot \begin{bmatrix} v_1 \\ L_1^m \\ v_2 \\ L_2^m \end{bmatrix} \tag{27}$$

where N_1 and N_2 are the shape functions. Now, with a time step, Δt, the virtual internal power is expressed as follows:

$$\delta P_{int} = \int_{\Omega} \sigma\, \delta \mathrm{L} + \bar{\sigma}^m \left(\delta \mathrm{L}^m - \delta \mathrm{L} \right) + \bar{\bar{\sigma}}^m \nabla(\delta \mathrm{L}^m)\ \mathrm{d}\Omega$$

$$= \int_{\Omega} \left[\delta \mathrm{L} \quad \delta (\mathrm{L}^m - \mathrm{L}) \quad \nabla(\delta \mathrm{L}^m) \right] \cdot \begin{bmatrix} \sigma \\ \bar{\sigma}^m \\ \bar{\bar{\sigma}}^m \end{bmatrix} \mathrm{d}\Omega \qquad (28)$$

$$= \int_{\Omega} (\boldsymbol{\delta d^e})^T \mathbf{Q}^{\mathrm{T}} \boldsymbol{\Sigma}\, \mathrm{d}\Omega$$

$$= \int_{\Omega} (\boldsymbol{\delta d^e})^T \mathbf{Q}^{\mathrm{T}} \mathbf{C} \mathbf{Q} \mathbf{d^e} \cdot \Delta t\, \mathrm{d}\Omega\ .$$

Finally, the conventional finite element method is used to solve the Eq.(28), step by step.

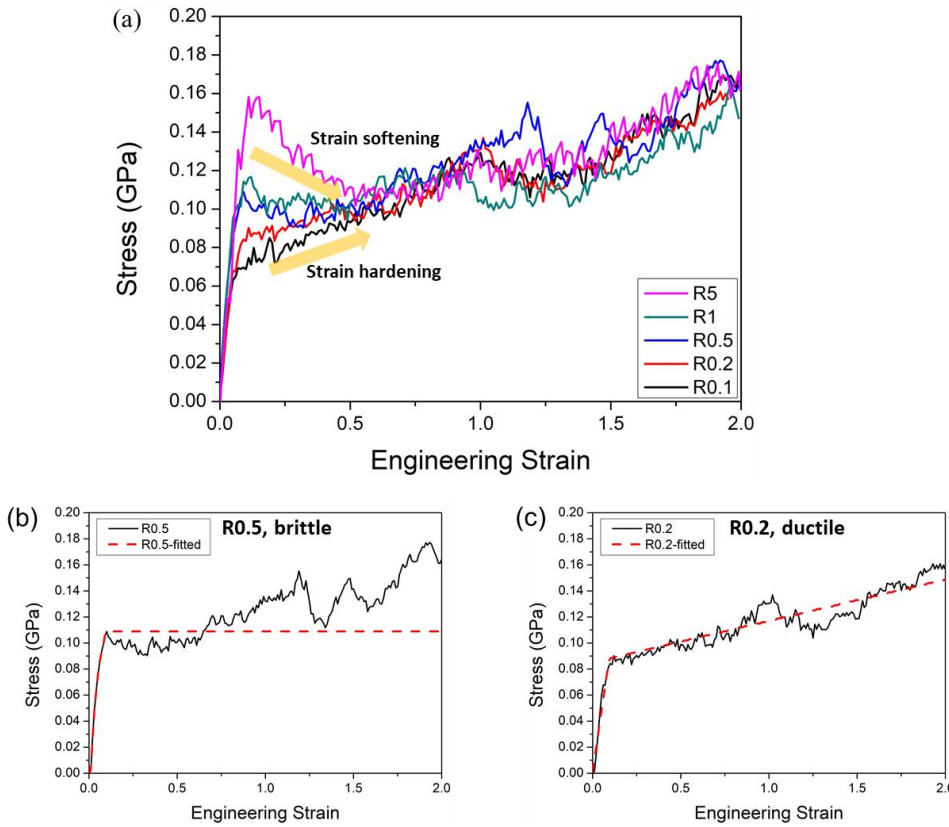

Figure 10. (a) S-s curves at 300K, 1 atm, and various strain rates. (b) is the raw R0.5 curve and a bilinear fit and (c) is the raw R0.2 curve and an elasto-plastic bilinear fit.

5. Results and discussions

5.1. Modification of MD results for the micromorphic theory

Figure 10(a) is the same s-s curve like Figure 3(a) except for an additional curve at a strain rate of R5. As discussed before, R0.5, R1, and R5 soften once they yield while R0.2 and R0.1 harden without showing any softening. Therefore, the ductile-brittle transition at 300K was determined between the two strain rates; R0.2 and R0.5. Now, their respective curves are going to be applied to the micro-scale of micromorphic theory model. The R0.5 curve represents the brittle s-s curve while the R0.2 curve represents the ductile s-s curve. The raw s-s curves are then substituted with a representative curve to make them applicable to the continuum formulation.

In Figure 10(b), the raw s-s curve of R0.5 is shown with a fitted line for use at the micromorphic theory. The fitted line starts with a linear elastic regime followed by the perfect plasticity. According to the literature, when crazing happens in a glassy polymer, the yielding is followed by a constant-stress drawing regime where the inborn crazes grow into a pillar-type structure [16, 19, 58, 59]. For this

reason, the post-yield behavior was fitted with a perfect plastic model. It is important to note that the hardening regime in the raw MD curve was neglected in the fitting because the current MD simulations disregard the bond scission. It has been confirmed that the end of the drawing regime corresponds to the onset of the bond scission [57]. Therefore, the strain hardening regime can be considered as the breaking regime, that is, the whole hardening regime can be considered as the perfect plasticity. The Young's modulus and the critical yield strain of the fit are 1.65GPa and 0.1, respectively.

Figure 10(c) shows the R0.2 curve with an elasto-plastic bilinear fit. As the s-s curve hardens right after the yield, a conventional bilinear fit is perfect to represent the raw MD curve [11]. The elasto-plastic model is defined by solving the optimization problem:

$$Minimize\ |r|, r(\sigma_Y, \epsilon_Y, \hbar) = \sigma^{R0.1} - f^{E-P}(\sigma_Y, \epsilon_Y, \hbar) \qquad (29)$$

where σ_Y, ϵ_Y, and $\hbar$ are yield stress, yield strain, and hardening parameter, respectively. $\sigma^{R0.1}$ and f^{E-P} are the raw MD curve and the bilinear fit, respectively. The fitted parameters are: σ_Y=85.2 MPa,

ϵ_Y = 0.09, and $\hbar$ = 32 MPa. It is worth noting that when a ductile deformation takes place, the bond scission was not observed in the current strain range [57, 60]. Thus no truncation was introduced in the ductile curve; the elasto-plastic bilinear fit is directly applied to the micromorphic model.

5.2. Macroscopic response of the ductile-brittle transition

The MD s-s curves are then applied to the micro-scale of the micromorphic model. Their input parameters are shown in Table 2 as micro-scale Young's modulus(E^m), hardening parameter(E^{tan}), and critical yield strain(ϵ_c^m). Length parameter of the micro-scale (l^m) is set as 10^{-5}mm to make the size of the micro-scale element comparable with that of MD RUC. Macro-scale Young's modulus(E) and yield stress(σ_Y) are taken from the experimental results in the literature [57]. The end-node velocity(v) and time-step(dt) are artificially chosen.

Table 2 Material parameters for the two-scale micromorphic theory. Macro-scale properties are from experimental results in the literature [57] while micro-scale properties are from MD simulations with fitted mechanical properties.

	E (MPa)	σ_Y (MPa)	l (mm)	E^m (MPa)	E^{tan} (MPa)	ϵ_c^m	l^m (mm)	v (mm/s)	dt (ms)
Brittle (R0.5)	1080	46	0.002	1650	0.001	0.1	10^{-5}	0.1	0.004
Ductile (R0.2)	1080	46	0.002	934	32	0.09	10^{-5}	0.1	0.004

.

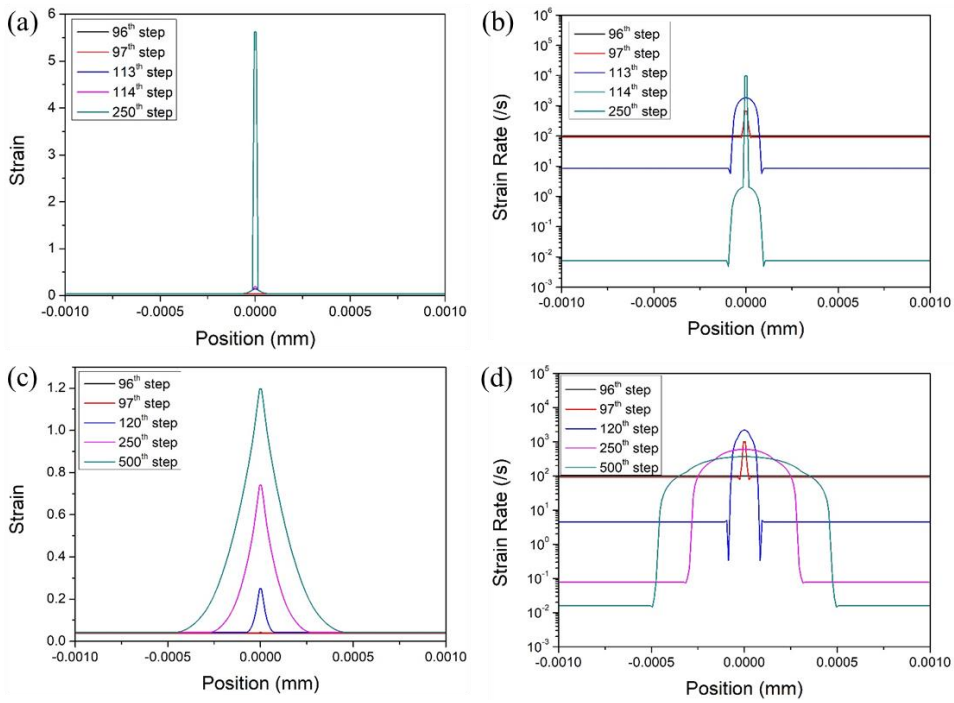

Figure 11. Strain and strain rate of brittle(a,b) and ductile(c,d) cases.

Figure 11 shows the results of the one-dimensional example of the two-scale micromorphic theory. Figure 11(a, b) are the brittle

case and Figure 11(c, d) are the ductile case. Figure 11(a,c) illustrates the elemental strain while Figure 11(b,d) shows the elemental strain rate which is calculated by dividing the strain increment by the time-step (dt). The results are taken at several time-steps which best demonstrate the macro-micro yielding transition of the elements

In early time steps, all elements are in the macro elastic regime and both the elemental strain and the strain rate are even for the entire position of elements. As can be seen in Figure 11(a,b), all elements are in the macro elastic regime until the 96th step. At 97^{th} time-step, the first macro yield happens at the mid-point elements since they are given with 10% less macro-scale yield stress. Starting from this time-step, the strain and strain rate distribution diverge from the even distribution along with the position. For instance, the mid-point elements start to endure more tensile strain and stretch faster than the other elements that are still in the macro-elastic regime. The macro yield then propagates to the nearby elements until the mid-point elements reach the micro-scale yield at 114^{th} step. Once they enter into the micro plastic regime with

near-zero tangent stiffness, they start to elongate a lot (take most of the elongation given) and fast. This is illustrated in Figure 11(b) that at this time-step, the strain rates of the mid-point elements and terminal elements that are still in the macro elastic regime are about 10^4 /s and 0.00751 /s, respectively. This tendency continues because once the mid-point elements enter into the micro plastic regime, the yielding pauses and the given stretch directly elongates the mid-point elements. Therefore, both 114th step and 250th step have the same strain rate.

Figure 11(c,d) shows the ductile case. The initial behavior is the same as the brittle case because the macro-scale properties are the same. However, once the mid-point elements encounter the macro-scale yield and enter into the micro-scale elastic regime, the strain and strain rate start to change. Especially when they reach the micro plastic regime, the tangent stiffness(E^{tan}) becomes 32 MPa while the brittle case was given with 0.001 MPa. Since the E^{tan} is higher than zero and lower than the micro-scale Young's modulus, all elements can stretch evenly. It is obvious that the elemental strain is the highest when an element is in the micro plastic regime and the lowest

when an element is in the macro elastic regime. Thus, the macro-scale yield spreads toward terminal elements as can be seen from 120^{th} to 250^{th} step in Figure 11(c,d). Finally, at 500^{th} step, approximately half the elements have passed the macro-scale yield. The same tendency is revealed in the strain rate. The strain rate gap between the elements in the macro elastic regime and the micro plastic regime is significantly small compared with the brittle case. Moreover, the mid-point elements' strain rate (3.66×10^2 /s) is approximately two orders of magnitude lower than the brittle case (10^4 /s). The relatively even stretch along the specimen demonstrates that the shear yielding is taking place in the ductile specimen while only a few elements endure the large and fast elongation in the brittle specimen.

In summary, the craze-type yielding occurs in the brittle case while shear yielding takes place in the ductile case. It is worth noting that the inputs from MD simulations are the stress-strain relationships, not the strain rates. Nonetheless, the micromorphic model returns quantitative data of elemental strain rates and the macro-scale behavior such as the shear yielding and the craze

yielding. This implies that with a careful calibration, a fully compatible combination of MD results and continuum models is available.

6. Conclusions and future works

6.1. Conclusions

The two-scale micromorphic theory that encompasses the experimental results and the MD simulations in a comparable length scale has been investigated. Since this thesis is a successive study of the former articles of our group [9, 57, 60], it is needed to start the conclusion from the origin of the discussion.

As mentioned in section 3.1, a realistic MD model that is grown from a mixture of monomers and initiators has been developed [16]. With this realistic model, the postulation that the MD RUC represents the nano-scale craze region has been demonstrated by matching the ductile-brittle transition of MD RUC and tensile specimens. The results yielded the strain rate of MD and the experiment becomes the same at the melting point, which indicates that the use of the MD approach needs to be restricted to the nano-scale region that endures the inhomogeneous plastic deformation. Thus a multi-scale model that can integrate both the macro-scale and the micro(or nano)-scale constitutive relationship should be used to utilize the MD tensile results properly; the micromorphic theory has been adopted.

The two-scale micromorphic theory that contains the tensile experimental results as the macro-scale constitutive relationship and the MD simulation results as the micro-scale constitutive relationship has been investigated. With a choice of the characteristic length parameter of the micro-scale, the continuum model became compatible in the length scale. Then the multi-scale model exhibited the distinctive ductile and brittle plastic deformation when given with ductile and brittle MD s-s curves respectively. Since it also yields the dynamic response from the s-s curves, the time-scale and the strain rate of the MD simulations and the continuum model can be comparable with a careful choice of model parameters.

6.2. Future works

In the future, the current one-dimensional model will be expanded to the three-dimensional case to investigate more realistic cases where the nano-scale defects (the mid-point elements in the one-dimensional example) are randomly distributed. Moreover, polymeric nanocomposites will be investigated by employing the multi-scale micromorphic model of which various nanoparticles are

assigned to each scale. At the same time, the coarse-graining MD simulations that can describe the large-scale nanocomposites are going to be studied.

Reference

1. Park, C. and G.J. Yun, *Characterization of Interfacial Properties of Graphene-Reinforced Polymer Nanocomposites by Molecular Dynamics-Shear Deformation Model.* Journal of Applied Mechanics, 2018. **85**(9): p. 091007.
2. Yang, S., J. Choi, and M. Cho, *Elastic stiffness and filler size effect of covalently grafted nanosilica polyimide composites: molecular dynamics study.* ACS Appl Mater Interfaces, 2012. **4**(9): p. 4792-9.
3. Khare, K.S. and R. Khare, *Effect of carbon nanotube dispersion on glass transition in cross-linked epoxy-carbon nanotube nanocomposites: Role of interfacial interactions.* The Journal of Physical Chemistry B, 2013. **117**(24): p. 7444-7454.
4. Jang, C., et al., *Molecular dynamics simulations of oxidized vapor-grown carbon nanofiber surface interactions with vinyl ester resin monomers.* Carbon, 2012. **50**(3): p. 748-760.
5. Park, C., J. Jung, and G.J. Yun, *Thermomechanical properties of mineralized nitrogen-doped carbon nanotube/polymer nanocomposites by molecular dynamics simulations.* Composites Part B: Engineering, 2019. **161**: p. 639-650.
6. Nouri, N. and S. Ziaei-Rad, *A molecular dynamics investigation on mechanical properties of cross-linked polymer networks.* Macromolecules, 2011. **44**(13): p. 5481-5489.
7. Park, C., J. Jung, and G. Yun, *Interfacial Characterization of Mineralized Carbon Nanotubes.* Composites Research, 2018. **31**(5): p. 282-287.
8. Zhu, F., C. Park, and G. Jin Yun, *An extended Mori-Tanaka micromechanics model for wavy CNT nanocomposites with interface damage.* Mechanics of Advanced Materials and Structures, 2019: p. 1-13.
9. PARK, C., et al. *A Polymer-physics-based Multiscale Modeling Approach for Inhomogeneous Deformation of Polymeric Nanocomposites*. in *Proceedings of the American Society for Composites—Thirty-fourth Technical Conference*. 2019.
10. Odegard, G.M., et al., *Predicting mechanical response of crosslinked epoxy using ReaxFF.* Chemical Physics Letters, 2014. **591**: p. 175-178.
11. Park, H., et al., *Toward the constitutive modeling of epoxy matrix: Temperature-accelerated quasi-static molecular simulations consistent with the experimental test.* Composites Part B: Engineering,

2018. **142**: p. 131-141.
12. Sahputra, I. and A. Echtermeyer, *Effects of temperature and strain rate on the deformation of amorphous polyethylene: a comparison between molecular dynamics simulations and experimental results.* Modelling and Simulation in Materials Science and Engineering, 2013. **21**(6): p. 065016.
13. Fotheringham, D. and B. Cherry, *The role of recovery forces in the deformation of linear polyethylene.* Journal of materials science, 1978. **13**(5): p. 951-964.
14. Akutagawa, K., et al., *Mesoscopic mechanical analysis of filled elastomer with 3D-finite element analysis and transmission electron microtomography.* Rubber Chemistry and Technology, 2008. **81**(2): p. 182-189.
15. Jaramillo, E., et al., *Energy-based yield criterion for PMMA from large-scale molecular dynamics simulations.* Physical Review B, 2012. **85**(2): p. 024114.
16. Jung, J., C. Park, and G.J. Yun, *Free Radical Polymerization Simulation and Molecular Entanglement Effect on Large Deformation Behavior.* European Polymer Journal, 2019.
17. Jung, J.-W., C.-W. Park, and G.-J. Yun, *Free Radical Polymerization Algorithm for a Thermoplastic Polymer Matrix: A Molecular Dynamics Study.* Composites Research, 2019. **32**(3): p. 163-169.
18. JUNG, J., et al. *Coarse-grained Molecular Dynamics Force Field for Carbon Black Filled Natural Rubber by Energy Renormalization Method*. in *Proceedings of the American Society for Composites—Thirty-fourth Technical Conference*. 2019.
19. Rottler, J. and M.O. Robbins, *Growth, microstructure, and failure of crazes in glassy polymers.* Physical Review E, 2003. **68**(1): p. 011801.
20. Venkatesan, S. and S. Basu, *Investigations into crazing in glassy amorphous polymers through molecular dynamics simulations.* Journal of the Mechanics and Physics of Solids, 2015. **77**: p. 123-145.
21. Matsushige, K., S. Radcliffe, and E. Baer, *The pressure and temperature effects on brittle-to-ductile transition in PS and PMMA.* Journal of Applied Polymer Science, 1976. **20**(7): p. 1853-1866.
22. Jang, B., D.R. Uhlmann, and J.V. Sande, *Ductile–brittle transition in polymers.* Journal of applied polymer science, 1984. **29**(11): p. 3409-3420.
23. Mahajan, D.K., B. Singh, and S. Basu, *Void nucleation and disentanglement in glassy amorphous polymers.* Physical Review E, 2010. **82**(1): p. 011803.
24. Sunyk, R. and P. Steinmann, *On higher gradients in continuum-atomistic modelling.* International Journal of Solids and Structures,

2003. **40**(24): p. 6877-6896.
25. Weinan, E. and P. Ming, *Cauchy–Born rule and the stability of crystalline solids: static problems.* Archive for Rational Mechanics and Analysis, 2007. **183**(2): p. 241-297.
26. Born, M. and K. Huang, *Dynamical theory of crystal lattices*. 1954: Clarendon press.
27. Murashima, T., S. Urata, and S. Li, *Coupling Finite Element Method with Large Scale Atomic/Molecular Massively Parallel Simulator (LAMMPS) for Hierarchical Multiscale Simulations.* arXiv preprint arXiv:1902.09171, 2019.
28. Urata, S. and S. Li, *A multiscale shear-transformation-zone (STZ) model and simulation of plasticity in amorphous solids.* Acta Materialia, 2018. **155**: p. 153-165.
29. Cosserat, E. and F. Cosserat, *Théorie des corps déformables.* 1909.
30. Toupin, R., *Elastic materials with couple-stresses.* 1962.
31. Mindlin, R.D., *Microstructure in linear elasticity*. 1963, COLUMBIA UNIV NEW YORK DEPT OF CIVIL ENGINEERING AND ENGINEERING MECHANICS.
32. Eringen, A.C., *Simple microfluids.* International Journal of Engineering Science, 1964. **2**(2): p. 205-217.
33. Eringen, A.C. *Theory of micropolar continua*. in *Proceedings of the Ninth Midwestern Conference*. 1965.
34. Wang, X. and J.D. Lee, *Micromorphic theory: a gateway to nano world.* International Journal of Smart and Nano Materials, 2010. **1**(2): p. 115-135.
35. Mazière, M. and S. Forest, *Strain gradient plasticity modeling and finite element simulation of Lüders band formation and propagation.* Continuum Mechanics and Thermodynamics, 2015. **27**(1-2): p. 83-104.
36. Hajidehi, M.R. and S. Stupkiewicz, *Gradient-enhanced model and its micromorphic regularization for simulation of Lüders-like bands in shape memory alloys.* International Journal of Solids and Structures, 2018. **135**: p. 208-218.
37. Li, S. and Q. Tong, *A concurrent multiscale micromorphic molecular dynamics.* Journal of Applied Physics, 2015. **117**(15): p. 154303.
38. Li, S. and S. Urata, *An atomistic-to-continuum molecular dynamics: Theory, algorithm, and applications.* Computer Methods in Applied Mechanics and Engineering, 2016. **306**: p. 452-478.
39. Germain, P., *The method of virtual power in continuum mechanics. Part 2: Microstructure.* SIAM Journal on Applied Mathematics, 1973. **25**(3): p. 556-575.
40. Eringen, A.C., *Balance laws of micromorphic mechanics.* International

Journal of Engineering Science, 1970. **8**(10): p. 819-828.
41. Vernerey, F., W.K. Liu, and B. Moran, *Multi-scale micromorphic theory for hierarchical materials.* Journal of the Mechanics and Physics of Solids, 2007. **55**(12): p. 2603-2651.
42. Vernerey, F.J., et al., *A micromorphic model for the multiple scale failure of heterogeneous materials.* Journal of the Mechanics and Physics of Solids, 2008. **56**(4): p. 1320-1347.
43. Liu, W.K., et al., *An introduction to computational nanomechanics and materials.* Computer methods in applied mechanics and engineering, 2004. **193**(17-20): p. 1529-1578.
44. Liu, W.K., E.G. Karpov, and H.S. Park, *Nano mechanics and materials: theory, multiscale methods and applications*. 2006: John Wiley & Sons.
45. Thompson, A.P., S.J. Plimpton, and W. Mattson, *General formulation of pressure and stress tensor for arbitrary many-body interaction potentials under periodic boundary conditions.* The Journal of chemical physics, 2009. **131**(15): p. 154107.
46. Hoover, W.G., *Canonical dynamics: equilibrium phase-space distributions.* Physical review A, 1985. **31**(3): p. 1695.
47. Stukowski, A., *Visualization and analysis of atomistic simulation data with OVITO–the Open Visualization Tool.* Modelling and Simulation in Materials Science and Engineering, 2009. **18**(1): p. 015012.
48. Rycroft, C.H., et al., *Analysis of granular flow in a pebble-bed nuclear reactor.* Physical review E, 2006. **74**(2): p. 021306.
49. Bennemann, C., et al., *Molecular-dynamics simulation of a glassy polymer melt: Rouse model and cage effect.* Computational and Theoretical Polymer Science, 1999. **9**(3-4): p. 217-226.
50. Paul, W., et al., *Chain motion in an unentangled polyethylene melt: A critical test of the rouse model by molecular dynamics simulations and neutron spin echo spectroscopy.* Physical review letters, 1998. **80**(11): p. 2346.
51. Kremer, K. and G.S. Grest, *Dynamics of entangled linear polymer melts: A molecular-dynamics simulation.* The Journal of Chemical Physics, 1990. **92**(8): p. 5057-5086.
52. Pütz, M., K. Kremer, and G.S. Grest, *What is the entanglement length in a polymer melt?* EPL (Europhysics Letters), 2000. **49**(6): p. 735.
53. Harmandaris, V., et al., *Crossover from the rouse to the entangled polymer melt regime: signals from long, detailed atomistic molecular dynamics simulations, supported by rheological experiments.* Macromolecules, 2003. **36**(4): p. 1376-1387.
54. Hossain, D., et al., *Molecular dynamics simulations of deformation mechanisms of amorphous polyethylene.* Polymer, 2010. **51**(25): p. 6071-6083.

55. Mahajan, D.K. and S. Basu, *On the simulation of uniaxial, compressive behavior of amorphous, glassy polymers with molecular dynamics.* International Journal of Applied Mechanics, 2010. **2**(03): p. 515-541.
56. Li, C. and A. Strachan, *Molecular dynamics predictions of thermal and mechanical properties of thermoset polymer EPON862/DETDA.* Polymer, 2011. **52**(13): p. 2920-2928.
57. Park, C., J. Jung, and G.J. Yun, *Multiscale micromorphic theory compatible with MD simulations in both time-scale and length-scale.* International Journal of Plasticity, 2020: p. 102680.
58. Venkatesan, S., et al., *Network approach towards understanding the crazing in glassy amorphous polymers.* Journal of Statistical Mechanics: Theory and Experiment, 2018. **2018**(4): p. 043305.
59. Baljon, A. and M.O. Robbins, *Simulations of crazing in polymer glasses: Effect of chain length and surface tension.* Macromolecules, 2001. **34**(12): p. 4200-4209.
60. Park, C., et al. *Multiscale Micromorphic Theory and Simulation with Co-existing Molecular and Continuum Time Scales*. in *AIAA Scitech 2020 Forum*. 2020.

국문초록

분자동역학과 마이크로몰픽 이론을 이용한 유리상 고분자의 멀티스케일 모델링 방법

박 찬 욱
항공우주공학과 항공우주공학전공
서울대학교 대학원

본 학위논문은 유리상 고분자에 대한 인장 실험과 분자동역학(MD) 시뮬레이션의 변형률 차이에 대한 분석으로 시작한다. 이를 위해 높은 변형률에서 수행 된 MD 인장 시뮬레이션이 실험 인장시편에서의 나노 스케일 크레이징(crazing) 영역을 나타낸다고 가정한다. 저자는 실험과 시뮬레이션에서 유리상 고분자의 연성-취성 전이를 비교함으로써, MD 시뮬레이션을 사용하여 유리상 고분자의 구성방정식을 도출하기 위해서는 마이크로(또는 나노) 스케일의 MD 결과를 통합 할 수 있는 멀티 스케일 접근법을 사용해야한다는 결론을 도출한다. 이를 위해 인장 실험과 MD 시뮬레이션을 통합 한 이중 스케일 마이크로몰픽 이론이 도입된다. 이중 스케일 마이크로몰픽 모델에서, 실험 결과는 매크로-스케일에 적

용되고 MD 결과는 마이크로-스케일에 적용된다. 이 멀티스케일 해석 방법에서는 특성 길이 상수를 조정하여 연속체 모델의 길이 스케일과 MD 시뮬레이션의 길이 스케일을 호환시킬 수 있다. 마지막으로, 이 모델은 연성 및 취성의 성질을 나타내는 MD 결과가 각각 마이크로몰픽 모델의 마이크로 스케일에 할당 될 때 연성 및 취성 변형의 거시적 거동을 성공적으로 예측한다. 제안된 멀티스케일 해석방법은 응력-인장률 커브로부터 동적인 반응을 반환하기 때문에 실험과 시뮬레이션의 시간 스케일 역시 모델 변수를 적당히 조절하여 호환 가능한 수준으로 만들 수 있다. 저자는 이러한 접근법이 MD 시뮬레이션과 연속체역학을 연결하기위한 새롭고 필수적인 접근법이 될 것으로 기대한다.

Keywords : **멀티스케일 시뮬레이션, 분자동역학, 유리상 고분자, 연성-취성 전이, 마이크로몰픽 이론**

Student Number : 2018-27299